Optics & Laser Technology 139 (2021) 106933

Contents lists available at ScienceDirect

Optics and Laser Technology

journal homepage: www.elsevier.com/locate/optlastec

Full length article

Sensitivity-enhanced temperature sensor based on encapsulated S-taper fiber Modal interferometer

Jianwen Ma [a], Shun Wu [a,*], Haihao Cheng [a], Xuemei Yang [a], Shun Wang [a], Peixiang Lu [a,b]

[a] Hubei Key Laboratory of Optical Information and Pattern Recognition, Wuhan Institute of Technology, Wuhan 430205, China
[b] School of Physics and Wuhan National Laboratory for Optoelectronics, Huazhong University of Science and Technology, Wuhan 430074, China

ARTICLE INFO

Keywords:
Optical fiber sensor
Temperature measurement
Integrated optical device
Modal interferometer

ABSTRACT

We demonstrated a simple technique for a highly sensitive temperature sensor based on an "S"-shape fiber taper Mach-Zehnder interferometer (MZI) with no need of special fibers or micromachining technique using high power lasers. To enhance the sensitivity, an S-shape single mode fiber (SMF) taper was encapsulated in a capillary filled with high thermos-optic coefficient liquid. We experimentally investigated the tuning parameters for the sensor, such as the taper shape, the material of the capillary, and the role of the filling liquid. Our results show a maximum sensitivity of −15.66 nm/°C in a measurement range of 28–32 °C, and −11.88 nm/°C from 25.1 °C to 35 °C for isopropanol sealed in Teflon capillary. The multi-interference model simulation shows that a critical cladding mode is responsible for the high sensitivity. Simple configuration, ease of fabrication, robustness and low cost make it suitable for high sensitivity temperature sensing applications.

1. Introduction

High-sensitivity temperature sensing measurement plays an important role in many fields, such as environmental science, biomedical and manufacturing industry. Compared to conventional electrical sensors, fiber-optic temperature sensors have been extensively studied owning to their intrinsic advantages of light weight, capability for remote sensing, and immunity to electromagnetic interference. In recent years, various types of fiber-based sensors have been demonstrated that enable temperature measurement, for example, fiber Bragg gratings [1–4], various configurations of modal interferometers [5–11], and new techniques such as surface plasmon resonance (SPR) [12,13]. Among these configurations, inline Mach-Zehnder interferometers (MZIs) have attracted a lot of research attentions due to their compact structure and ease of fabrication. In most MZIs designs, however, since both the core and cladding modes involved in the interference mainly propagate in the same material silica, the relative difference of the thermo-optic coefficient is small, resulting in a low sensitivity of tens of pm/°C [9,10], or hundreds of picometers per degree [11] when using some special fibers.

One way to enhance the sensitivity for an MZI sensor is to create large difference in thermo-optical coefficient between the fiber core and cladding. There are several ways to achieve this. One can use special fiber, for example, few-mode multicore fiber [14], or artificially create such conditions by selectively infiltrating liquids with high thermo-optic coefficient [15,16]. Although the sensitivity can reach 40–55 nm/°C, they suffer from narrow measurement range. Moreover, these configurations usually require micromachining using high power femtosecond lasers.

Considering fabrication complexity and cost, infiltrating liquids into a capillary is an effective method to realize a simple and compact structure with high sensitivity and moderate measurement range. Yang et al. reported sealing an S-shape fiber taper with refractive index (RI) liquid inside a silica capillary, and obtained a sensitivity of 1.403 nm/°C [17]. Xue et al. showed an improved sensitivity of −3.88 nm/°C by filling isopropanol in an optical microfiber taper-based MZI [18]. More recently, Jiang et al. developed an optical microfiber coupler with RI liquid encapsulated in Teflon capillary, with a sensitivity of −5.3 nm/°C reported [19]. A technical disadvantage for these microfiber couplers is that the waist diameter is limited to only a few microns, which makes the device fragile and brings challenge for packaging. Moreover, the papers mentioned above did not explain their results theoretically in aspect of the interference modes.

In this paper, we proposed and demonstrated a compact in-line fiber-optic temperature sensor based on multimode interference. We carefully optimized several parameters for achieving high sensitivity: the length and waist of the single mode S-taper, the material of the capillary, and

* Corresponding author.
E-mail addresses: wushun_wit@163.com, wushun@wit.edu.cn (S. Wu).

https://doi.org/10.1016/j.optlastec.2021.106933
Received 11 September 2020; Received in revised form 5 January 2021; Accepted 10 January 2021
Available online 12 February 2021

the filling liquid. The experimental results showed that the highest temperature sensitivity of −15.66 nm/°C with high linearity (R^2 = 0.993) was obtained for as S-taper encapsulated with isopropanol in a Teflon capillary, with a temperature range of 28–32 °C. In a larger range of 25.1–35 °C, the sensitivity was −11.88 nm/°C. This is at least an enhancement of compared with other capillary infiltrated temperature sensors reported [17–19]. In addition, we also studied the underline mechanism for achieving such high sensitivity. Our numerical simulation showed there existed a critical cladding mode for a single mode fiber. When the cladding mode involved in the interference with the core mode is close to the critical mode, the sensor exhibits the highest sensitivity. In addition, given the interference cladding mode, the direction for the wavelength shift when temperature varies can be determined. The calculated results were consistent with our experimental observation. The merits of compactness, robustness, and ease to production make the proposed temperature sensor a strong candidate for high sensitivity near room temperature measurement in applications including industrial production and environmental monitoring.

2. Sensor principle and theory

The proposed temperature sensor consists of two parts: the main part was an S-shape tapered SMF, as illustrated in Fig. 1(a-b). The taper was then encapsulated with RI liquid inside a Teflon capillary. Unlike normal tapers, two curvatures were created in one S-taper to form the MZI. At the first bend, multiple cladding modes are excited. After travelling a certain distance along the waist, these cladding modes were coupled back into the fiber core and combine with the core mode at the second bend. Thus, a typical MZI was formed. The transmission spectrum is a result of multimode interference among the core mode and a number of excited cladding modes. As shown in Fig. 1(c), a nearly-defined FSR was obtained implying that there exists a dominant interference. The shape of the S-taper has an effect on the interference spectrum because it determines the efficiency for the cladding modes excitement and power distribution of the core and cladding modes. The resulting interference intensity can be written as [20]:

$$I = I_{co} + \sum_m I_{cl}^m + \sum_m 2\sqrt{I_{co}\cdot I_{cl}^m}\cdot cos\phi^m \quad (1)$$

Here, m is the order number. Subscript co and cl denote for core and cladding. ϕ^m is the phase delay between core mode and m^{th}-order cladding mode, which is:

$$\phi^m = \frac{2\pi\Delta n_m^{\mathrm{eff}} L_{\mathrm{eff}}}{\lambda} \quad (2)$$

where $\Delta n_m^{eff} = n_{co}^{eff} - n_{cl,m}^{eff}$ is the effective refractive index (ERI) difference between core mode and m^{th}-order cladding mode. λ and L_{eff} represent the wavelength and the effective interference length for the taper. As the external temperature changes, the RI of the sealed liquid varies, leading to a variation in accumulated phase between the two inferencing modes.

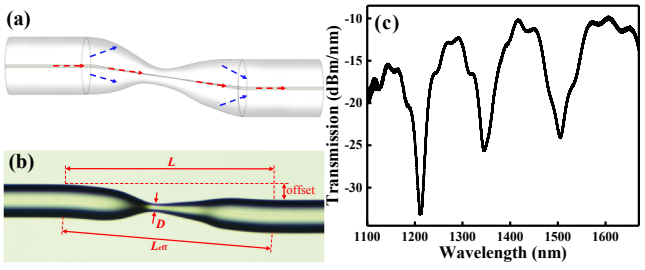

Fig. 1. (a) Schematic diagram and (b) micrograph picture of the S-taper structure. L and D represents the taper length and waist, respectively. The effective interference length L_{eff} is along the taper direction and slightly larger than L. (c) Transmission spectrum for an S-taper in air.

To quantitatively analyze the transmission spectrum, we solved the transcendental equation [21] and plotted the ERI of the core mode and the first twenty $HE_{cl,m}$ cladding modes in wavelength range of 1000–1600 nm, shown in Fig. 2(a), m = 1 represents the first cladding mode. In the calculation, SMF is considered as a three-layer structure of core, cladding and external environment. The radius (RI) of the core and cladding were set to be 4.07 μm (1.45205) and 62.5 μm (1.44681), respectively. The calculated ERI for the fundamental core mode at 1550 nm was 1.44904, which agreed well with the modal field plot of SMF using the same value in COMSOL, as shown in the inset of Fig. 2(a).

The sensitivity of a particular interference dip is an overall effect of

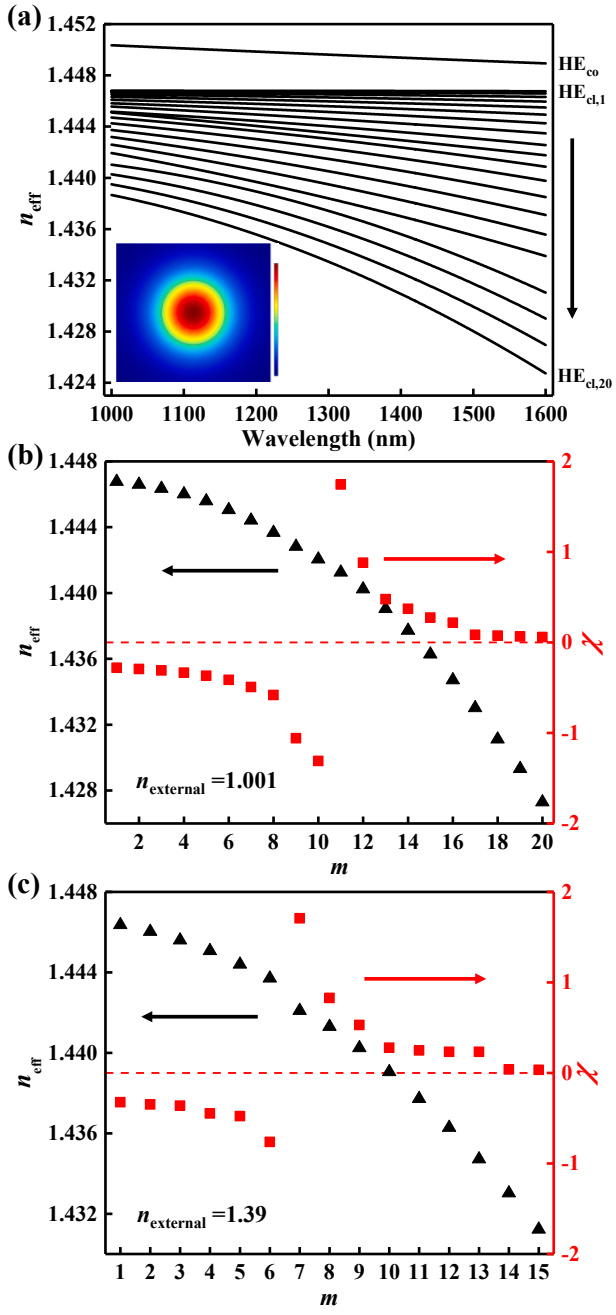

Fig. 2. (a) The ERI versus wavelength for the core mode and the first twenty $HE_{cl,m}$ cladding modes when external environment is 1.001. The inset shows a modal field for the fundamental core mode in SMF. The ERI (black triangles) and sensitivity coefficient (red squares) corresponding to (b) the first twenty $HE_{cl,m}$ cladding modes when the SMF is exposed in air and (c) the first fifteen $HE_{cl,m}$ cladding modes when the external RI is 1.39.

all interferences, which include both core-cladding and cladding-cladding interferences. However, the major interference dips are caused by core-cladding interferences. This is because the difference in the ERI between the core mode and a cladding mode matches the nearly-defined FSR, indicating that the major interference is between the core mode and a dominate cladding mode. Meanwhile, the ERI differences between any two cladding modes are small, corresponding to a much large FSR. Therefore, interferences related to weakly excited cladding modes only cause slight intensity modulation on the main interference pattern. According to Ref. [22], the sensitivity for a certain interference dip resulting from a core-cladding interference can be expressed as the product of two terms:

$$\frac{d\lambda_{dip,i}}{dn_{ex}} = \chi \frac{\partial n_{cl,m}^{eff}}{\partial n_{ex}} \tag{3}$$

$$\chi = -\frac{\lambda_{dip,i}}{\Delta n_m^{eff}} \Big/ \left[1 - \frac{\lambda_{dip,i}}{\Delta n_m^{eff}} \left(\frac{\partial n_{co}^{eff}}{\partial \lambda} - \frac{\partial n_{cl,m}^{eff}}{\partial \lambda}\right)\right] \tag{4}$$

The subscript i denotes for the i^{th} interference dip. In Eq. (3), χ is defined as the sensitivity coefficient of core-cladding interference, and the partial derivative quantifies the dependence of the ERI of the m^{th} cladding mode on the external RI, which was found positive for general $HE_{cl,m}$ cladding modes at wavelength of 1550 nm in air (not shown). As a result, the direction for the wavelength shift of the interference dip depends solely on the sign of χ. In Fig. 2(b), both the ERI (black triangles) and the sensitivity coefficient χ (red squares) were plotted for the first twenty $HE_{cl,m}$ cladding modes at wavelength of 1550 nm, when the SMF was exposed in air. Two trends were evident in Fig. 2(b): the ERI became smaller for higher-order cladding modes; moreover, there existed a critical cladding mode around which the magnitude of χ reached maximum. When the fundamental core mode interferes with a higher-order cladding mode that is below the critical mode, e.g. $HE_{cl,10}$, the interference dips would experience blue shift as the ambient RI increased. In contrary, when a higher-order mode above the critical mode, e.g. $HE_{cl,13}$, is involved in the interference, the dips would experience red shift. This result was consistent with the analysis in Ref [22].

The magnitude of the sensitivity for a particular dip is more complicated to predict. According to above theory, it depends on the product of two quantities on the right-hand side of Eq. (3). The sensitivity coefficient χ was calculated in Fig. 2(b). We also calculated the partial derivative for the cladding modes, but only at 1550 nm. The preliminary result showed that this quantity was almost the same value for all the first twenty cladding modes (not shown), except for a largest value when $m = 10$. Considering both quantities, we have confidence to conclude that it is preferable to excite cladding modes as close to the critical modes as possible, in which case it is more likely to have a larger RI sensitivity.

Fig. 2(c) shows the ERI (black triangles) and the sensitivity coefficient χ when the external RI is changed to 1.39. A noticeable change is that the critical cladding mode is shifted to lower order (m = 6 or 7). This result can be explained as follows: The sign of the coefficient depends on the relative slope of the effective refractive index (ERI) of cladding mode with respect to that of the core mode. The slope of ERI of the core mode $\partial n_{co}^{eff}/\partial\lambda$ is negative as shown in Fig. 2(a), while $\partial n_{cl,m}^{eff}/\partial\lambda$ starts with a small negative value for lower order cladding modes and decreases to a more negative value for higher order cladding modes. When $\left|\partial n_{cl,m}^{eff}/\partial\lambda\right| < \left|\partial n_{co}^{eff}/\partial\lambda\right|$ or $\lambda_{dip,i}(\partial n_{co}^{eff}/\partial\lambda - \partial n_{cl,m}^{eff}/\partial\lambda)/\Delta n_{eff,m} < 1$, χ is negative. Only when the condition $\lambda(\partial n_{co}^{eff}/\partial\lambda - \partial n_{cl,m}^{eff}/\partial\lambda)/\Delta n_{eff,m} > 1$ is satisfied, χbecomes positive. The corresponding cladding mode at this turning point is the critical cladding mode. When the external RI increases to 1.39, $\partial n_{co}^{eff}/\partial\lambda$ remains the same but the $\partial n_{cl,m}^{eff}/\partial\lambda$ decreases faster. Therefore, a smaller m order is required to reach the same value of $\partial n_{co}^{eff}/\partial\lambda - \partial n_{cl,m}^{eff}/\partial\lambda$, indicating that the critical cladding mode becomes smaller for higher external RI.

3. Sensor fabrication

The S-taper was fabricated by a commercial fusion splicer (Fujikura 80S) using two SMFs. We started off by separating the two fibers with a ~62 μm offset in the vertical direction. During splicing, the fibers were stretched outwards to create the tapering shape. A number of tapering parameters have been tried to optimize the shape of the taper, such as tapering speed, tapering length, arc current, and arc duration. Our results show that the shape of the S-taper is most sensitive to two parameters for controlling the tapering length L and the waist diameter D: tapering speed and tapering length. Useful criteria for optimization include the spectral shape, mechanical strength, and reproducibility. We found that for each tapering sped, there exists a corresponding maximum tapering length. For example, when we increased the tapering speed from 10 bit to 100bit, the maximum tapering length is increased from 240 μm to 360 μm. When the tapering waist is small, the efficiency of cladding mode excitement is high, but it is more difficult to reproduce the taper and the sensor becomes fragile. Another consideration is the transmission spectrum. For each set of tapering parameters, we aimed at obtaining a transmission spectrum with clean interference dips with high contrast ratio. Based on the above considerations, we choose a tapering speed of 25 bit and a tapering length of 270 μm as the final recipe for S-taper. Due to the asymmetrical movement of the motor, the produced taper usually has a non-symmetric shape, as shown in Fig. 1 (b). In our experiment, L (D) was chosen to be between 690–850 μm (28–40 μm). Later, the taper structure was inserted into a capillary, followed by filling liquid of high thermal-optic coefficient. The sensor was then completed by a tight sealing with glue. During the temperature test, we found it was essential to avoid trapping air inside the capillary. Because even a small amount of air would expand to bubbles at high temperatures, whose movement could lead to an unstable transmission spectrum. To prevent leakage, both ends was secured twice: we applied AB glue after the UV glue was dried.

4. Experimental results and discussion

The experimental setup for the temperature sensing test was illustrated in Fig. 3. The sealed sensor was placed inside a column oven with accuracy of 0.1 °C. We used a broadband source (BBS, YSL, 900–1700 nm) as the input light source, which passed through the proposed sensor and was received by an optical spectrum analyzer (OSA, YOKOGAWA AQ6370B).

4.1. Mode analysis for different taper configurations

The first step was to investigate how the cladding modes were excited for different taper configurations. Three tapers T1-T3 were fabricated as shown in Table 1, corresponding to the splicer tapering length setting of 250, 260 and 270 μm, respectively. We measured the transmission spectra for the three tapers exposed in air at room temperature, plotted in black curves in Fig. 4. The spectra consisted of several regularly-spaced dips, which were from multimode interference.

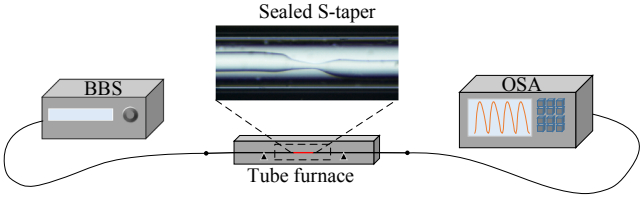

Fig. 3. Schematic diagram of the experimental setup for temperature measurement. BBS: broadband source, OSA: optical spectrum analyzer. The inset shows an S-taper sealed in a silica capillary with RI liquid.

Table 1
Parameters of three S-taper structures.

Taper	Splicer setting		Geometrical parameters		
	Offset (μm)	Tapering length (μm)	*L* (μm)	*D* (μm)	Offset (μm)
T1	62.4	250	697	39.2	51.0
T2	62.4	260	776	37.2	64.7
T3	62.4	270	835	29.4	56.8

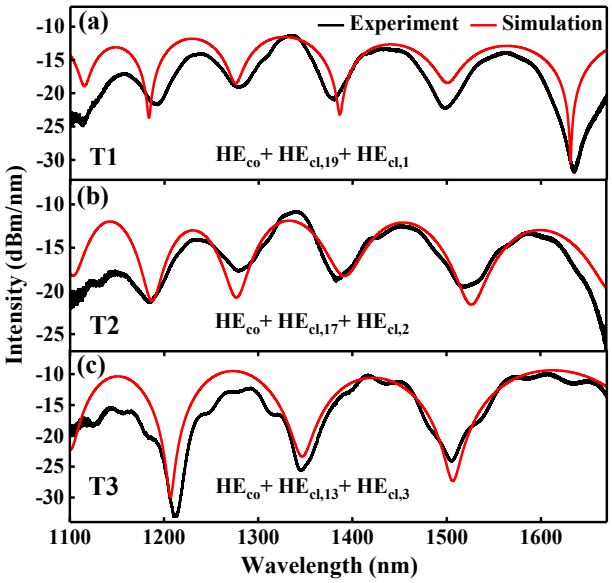

Fig. 4. Comparison of experimentally measured (black) and simulated (red) transmission spectra of the tapered structure (a) T1, (b) T2, and (c) T3 measured in air.

For simplicity, we only considered interferences among the core mode and two of the first twenty cladding modes in our simulation. The results were represented by the red curves, which agreed well with the experimental spectra. It was found that in all cases, the transmission spectra were mainly determined by two contributions: a dominant interference between the core mode and a high-order cladding mode, giving rise to the relatively small FSR; and a minor interference between the core mode and a lower-order cladding mode, which formed an envelope with large FSR on top of the spectra. For example, in Fig. 4(a), the 19th cladding mode interfered with the core mode, leading to the six transmission dips, while the first cladding mode interfere with the core mode and caused the overall intensity variation. As the tapering length increased from 250 to 270 μm, larger FSR for the interference dips was observed, suggesting that lower-order cladding mode were more likely to be excited in the dominant interference.

The wavelength shift for a particular transmission dip was a combination of different interference channels. For all the three spectra, the cladding modes $HE_{cl,19}$, $HE_{cl,17}$, and $HE_{cl,13}$ responsible for the major interference, which are above the critical mode ($HE_{cl,10}$), have positive χ according to Fig. 2(b). This indicates that these interference dips would experience red shift as the external RI increases. Meanwhile, for the minor interference, $HE_{cl,1}$, $HE_{cl,2}$, and $HE_{cl,3}$ were all below the critical mode, and would give a blue shift and counteract part of the red shift induced by the former interference. Among the three higher-order cladding modes, $HE_{cl,13}$ was the closest to the critical mode, and had the largest positive χ value. Moreover, Fig. 2(b) indicated that $HE_{cl,1}$, $HE_{cl,2}$, and $HE_{cl,3}$ have almost the same χ. T3 was therefore expected to have a higher RI sensitivity than T1 and T2.

4.2. Temperature performance in silica capillary

After we measured the transmission spectra in air, S-taper T1, T2 and T3 were encapsulated with high thermo-coefficient RI liquid (n = 1.39) into three separate silica capillaries for temperature performance test. The silica capillaries have inner (outer) diameter of 320 μm (425 μm). These three samples were denoted as S1, S2 and S3, respectively. When the surrounding RI changes from air to RI liquid, the effective RI of the cladding mode also varies, leading to a new refractive index distribution at the taper waist. Since the efficiency for the cladding mode excitement is determined by the waveguide structure, the power distribution of the core and cladding modes change accordingly. This causes variation in the major cladding mode involved in the interference. During the test, the temperature was gradually increased from 30 °C to 65 °C at a step of 5 °C. All spectra were recorded ten minutes after the temperature was stable. Since the thermo-optical coefficient of RI liquids is negative, as temperature increases, the RI of the liquid would decrease, leading to a blue shift for the interference dips as the spectral changes of S3 shown in Fig. 5(a). These experimental observations were in accordance with the characteristic tendency observed in Fig. 2 (b) for S-tapers in air, indicating that the excited cladding mode for S3 taper is closer to the corresponding critical mode than that for S1 and S2. The linear fitting of the

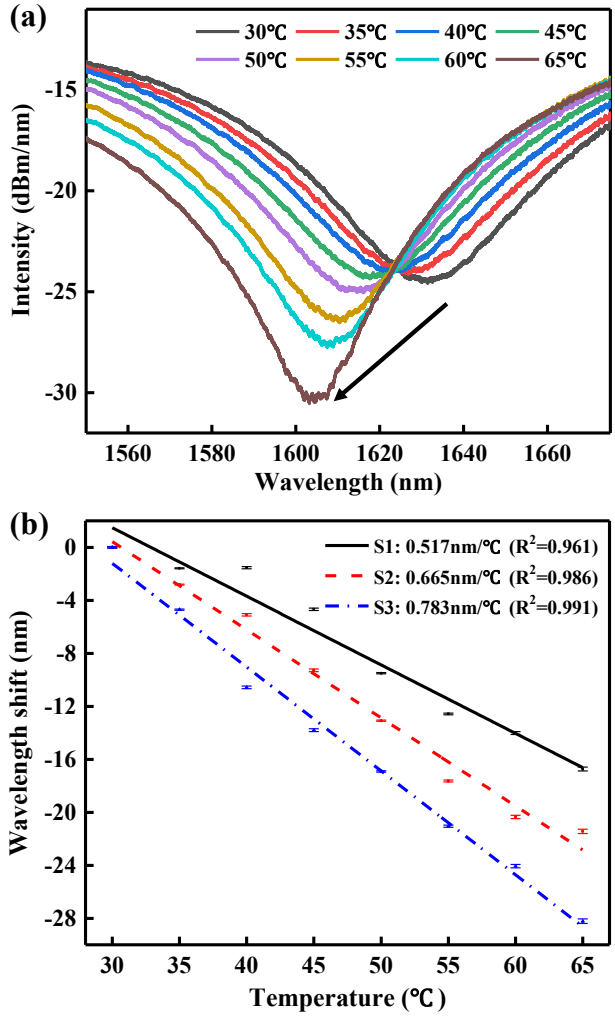

Fig. 5. (a) Transmission spectra of S3 at different temperature. (b) Comparison of the temperature sensing performance for dip near 1600 nm: S1 (black solid line), S2 (red dotted line) and S3 (blue dotted triangle). An offset of 1646.6 nm (S1), 1649.0 nm (S2), and 1631.4 nm (S3) is subtracted in y axis for direct comparison of slopes.

wavelength shift shown in Fig. 5(b) gave a temperature sensitivity of −0.517 nm/°C, −0.665 nm/°C, and −0.783 nm/°C for S1, S2 and S3, respectively. Among the three, S3 had the highest sensitivity. Therefore, taper T3 was employed in all later experiments. The error bars for all data points were also included indicating a small wavelength uncertainty in silica capillaries. For example, the uncertainty for S3 is ±0.23 nm around 1632.95 nm.

4.3. Temperature performance in Teflon capillary

For further characterization, we investigated the role for the capillary. Since Teflon has a higher thermal expansion coefficient of 0.8 × 10^{-4}/°C [23] compared with silica of 5.5 × 10^{-7}/°C [23], when temperature increases, thermal-expansion effect occurs in addition to the thermal-optic effect. The resulting consequence is that the expansion causes strain along the axial direction of the S-taper. Both effects will lead to wavelength shift of the interference dips. In order to investigate the direction of the wavelength shift due to thermal-expansion, we conducted an experiment to study the shift direction in response to axial strain along the fiber. The strain was applied for a given S-taper in air by stretching the S-taper outwards using translation stages. Our results were shown in Fig. 6. The transmission spectrum exhibited a blue shift with the sensitivity of −51.2 pm/$\mu\varepsilon$. This is the same direction as the shift caused by the RI liquid.

Sample S4 used the same taper T3 but encapsulated in a Teflon capillary with inner (outer) diameter of 1.5 mm (1.9 mm). From the fabrication point of view, it was quite reproducible for making T3 tapers and obtain similar temperature sensing behavior. However, we found that sometimes the sensors had similar sensitivity, but the dips exhibited wavelength shift for opposite directions. Such cases were shown in Fig. 7 (a) and (c), in which two sensors S4-A and S4-B were made under exactly the same condition. In Fig. 7, we compared the temperature sensing performance and found they had similar sensitivity. The data we obtained were not as linear as the results in silica capillary. In Fig. 7(b) and (d), second order polynomial fit showed the maximum sensitivity was −7.08 and 7.65 nm/°C for sensor S4-A and S4-B, respectively. This was a factor of ten improvement over the results we obtained in silica capillary.

The underline mechanism for the "opposite shift" behavior could be explained by our "critical mode" model. Fig. 8 showed the comparison between the simulation and the measured spectrum for sensor S4-B, we found that the dominant cladding mode involved in the interference with the core mode was $HE_{cl,5}$, which was very close to the critical mode at presence of the RI liquid shown in Fig. 2(c). When the excited cladding mode was close to the critical mode, it might have some uncertainty in exciting cladding mode lower or higher than the critical mode.

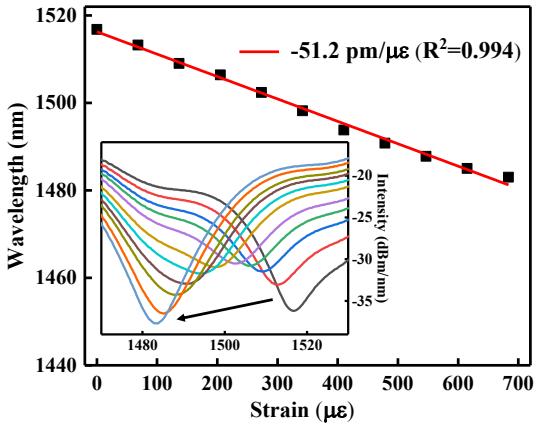

Fig. 6. Blue shift of the S-taper interference dip around 1515 nm in response to axial strain in air. Inset shows the transmission spectra of T3 under different amount of strain.

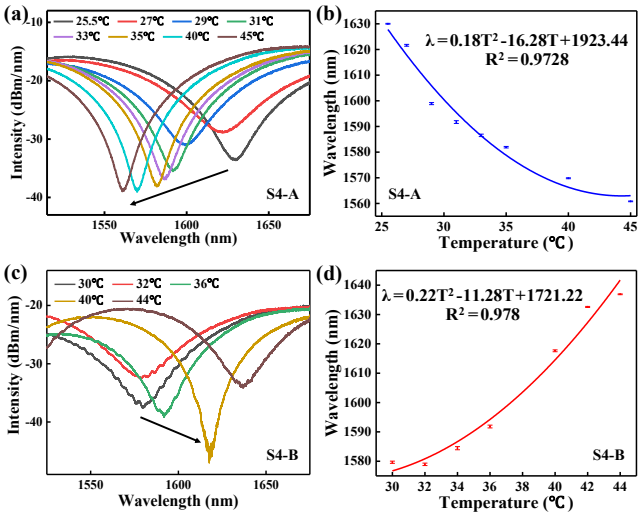

Fig. 7. Temperature measurements for two identical S4 tapers packaged in Teflon capillary (ID = 1.5 mm). RI liquid (n = 1.39) was filled into the capillary. Two sensors showed opposite wavelength shifts. (a) The transmission spectra and (b) the dip wavelength shift as a function of temperature for sensor S4-A, and (c) the transmission spectra and (d) the dip wavelength shift as a function of temperature for sensor S4-B.

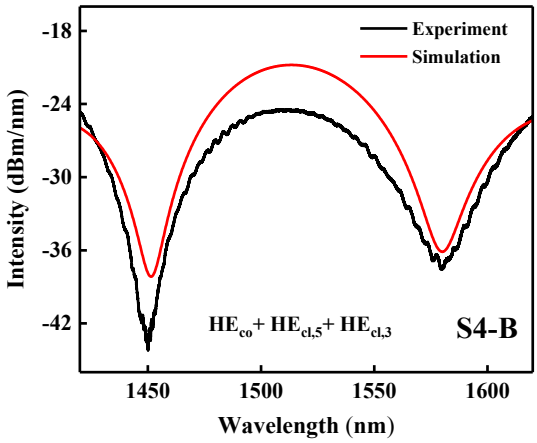

Fig. 8. Comparison of the simulated with the measured transmission spectrum for S4-B.

Nevertheless, in either case, the sensor was very likely to have a high sensitivity.

4.4. Temperature performance with isopropanol

Since isopropanol has a higher thermo-optic coefficient of −4.5 × 10^{-4}/°C [24], and a high thermo-expansion coefficient of 1.07 × 10^{-3}/°C, we replaced the RI liquid by isopropanol, with all other parameters remained the same as S4. Fig. 9 illustrates the spectra response of two such sensors S5-A and S5-B when the temperature increased from 25.1 °C to 35 °C. Fig. 9(a) shows the temperature sensitivity of an interference dip at 1370 nm, which is −7.60 nm/°C and −7.57 nm/°C for the heating and cooling process, respectively. The maximum difference in wavelength variation is 4.8 nm (at 30 °C) during the heating and cooling process. In Fig. 9(b), the sensitivity for the resonance dip around 1620 nm has a significant improvement over the RI liquid. The linear fitting of the overall data gave a sensitivity of −11.88 nm/°C with an R^2 value of 0.982. The steepest slope indicated an even higher sensitivity of −15.66 nm/°C with R^2 equals to 0.993, however, in narrower range of 28 to 32

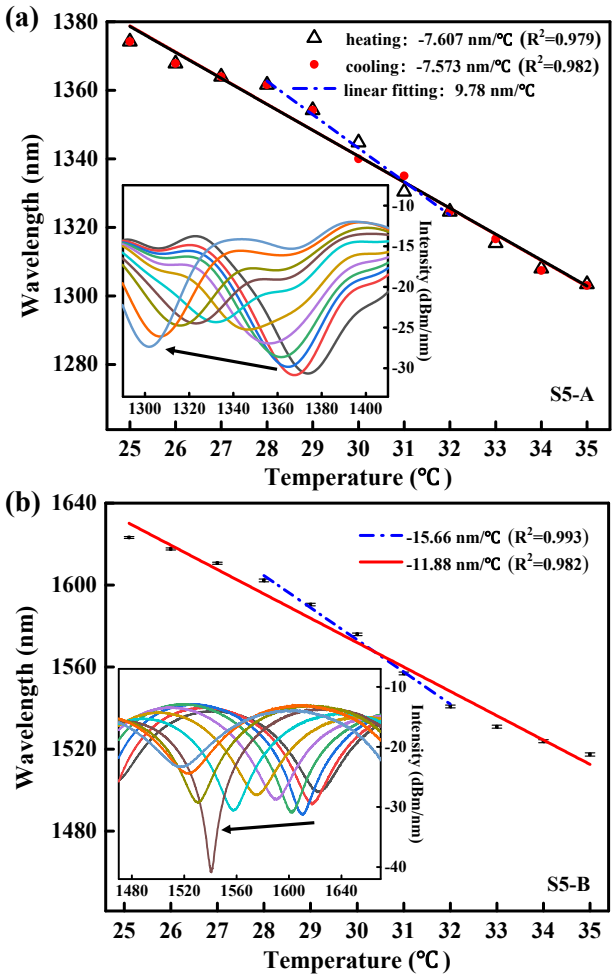

Fig. 9. Temperature response for two S5 sensors packaged in Teflon capillary (ID = 1.5 mm) filled with isopropanol. Insets show the corresponding transmission spectra at various temperatures. Wavelength shift for interference dip of (a) S5-A around 1370 nm, and (b) S5-B around 1620 nm.

°C. During the heating process, the intensity of the interference dip varied by about 8 dB over 10 °C except that at 32 °C, the intensity suddenly dropped 9 dB. The average intensity modulation sensitivity is about 1.7 dB/°C.

The discrepancy in the sensitivity for S5-A and S5-B is because the sensitivity is wavelength dependent. Fig. 10(a) shows the temperature sensitivities for different interference dips from S5-A and S5-B. There is an obvious trend that the sensitivity is higher for longer wavelength dips. This result accords with sensitivity measurements from both sensors. For real implementation of high sensitivity sensors, one can use a fusion splicer with precise tapering control, and an infrared camera to monitor the transmission spectrum during the tapering process [29]

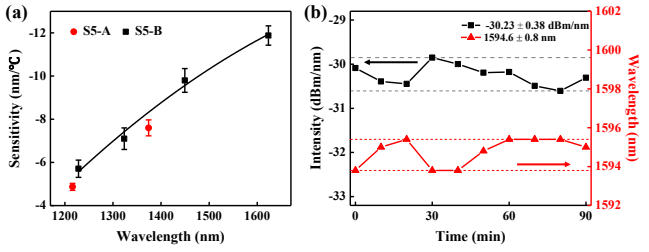

Fig. 10. (a) The relationship between the sensitivity and wavelength. (b) The intensity versus time at 35 °C.

such that a favorable interference dip at longer wavelength can be achieved. Moreover, we evaluated the stability of the sensor by measuring the wavelength and power fluctuations. Fig. 10(b) shows that during 90 min, the wavelength fluctuation is ±0.38 dB, while the power fluctuation is ±0.8 nm. The power stability was similar for Teflon configurations either filled with RI liquid or isopropanol. Compared to silica capillary, Teflon has almost twice the wavelength fluctuation, and over ten times the power fluctuation than silica, probably due to its large thermal-expansion coefficient.

A comparison with earlier work in Table 2 showed that the performance of our sensor in terms of sensitivity was more superior than other fiber temperature sensors by at least a factor of two. Compared to the sensors which required special techniques, such as coating thin film or microfiber machining using femtosecond laser, our design has advantages of robustness, lower in complexity, and hence less manufacturing difficulty and cost. These features make our proposed sensor suitable for many high sensitivity temperature sensing applications, including healthcare, biological sensing field, consumer electronics and etc.

5. Conclusions

In summary, we have demonstrated the simple design for an inline fiber interferometer as a highly sensitive temperature sensor based on encapsulated S-taper fiber filled with liquids. The multi-interference model explains the underlying physics behind the high sensitivity. We found that there existed a critical cladding mode, dependent on the external RI. When the excited cladding mode involved in the interference with the core mode was close to the critical mode, the sensor was likely to exhibit high sensitivity. Given the cladding mode number, the direction of the wavelength shift with temperature could be determined. This agreed well with our experimental observations.

In the experiment, the performances for various taper configurations the material of capillary, and the filling liquids were systematically investigated. Our results showed that a long and thin S-taper was favorable for achieving high sensitivity. Capillary material with higher thermos expansion coefficient and filling liquid with high thermal-optic coefficient were preferred. The maximum temperature sensitivity we obtained was −15.66 nm/°C with measurement range from 28 °C to 32 °C for a transmission dip at around 1630 nm, based on an S-taper with isopropanol sealed in a Teflon capillary. In a larger range of 25.1 °C to 35 °C, the sensitivity was measured to be −11.88 nm/°C. This was at least a factor of two enhancement compared to previously reported capillary infiltrated temperature sensors. We offered a simple solution for temperature measurement with high sensitivity. The combined compactness and robustness of our sensor implies applications in many fields such as environmental monitoring, biomedical applications and industrial production.

CRediT authorship contribution statement

Jianwen Ma: Conceptualization, Methodology, Software, Formal

Table 2
Comparison with other optical fiber temperature sensors.

Ref	Sensor type	Sensitivity (Temp range) nm/°C (°C)
[19]	Packaged OMC filled with liquids	−5.3 (35–45)
[18]	Isopropanol-sealed OMT	−3.88 (20–50)
[16]	Selectively infiltrated PCF	54.3 (34–35.4)
[12]	SPR-based temperature sensor	−4.13 to −82.07 (20–70)
[25]	MZI with side-opened channels	3.8 (22–34)
[26]	hybrid waveguides based MZI	0.172 (24.1–31.8)
[27]	Liquid core fiber interferometer	−0.0427 (25–80)
[28]	PDMS wrapped CSPF	−0.4409 (35–85)
This work	Packaged STF filled with isopropanol	−11.88 (25.1–35) −15.66 (28–32)

analysis, Writing - original draft. **Shun Wu:** Data curation, Formal analysis, Writing - original draft, Writing - review & editing. **Haihao Cheng:** Software, Validation. **Xuemei Yang:** Software, Validation. **Shun Wang:** Validation, Writing - review & editing. **Peixiang Lu:** Supervision.

Declaration of Competing Interest

The authors declare that they have no known competing financial interests or personal relationships that could have appeared to influence the work reported in this paper.

Acknowledgments

This work is supported by grants from Natural Science Foundation of China (NSFC) (61805182, 11804258).

References

[1] Y. Dong, S.Y. Xiao, B.L. Wu, H. Xiao, S.S. Jian, Refractive index and temperature sensor based on D-shaped fiber combined with a fiber bragg grating, IEEE Sens. J. 19 (4) (2018) 1362–1367.
[2] S.J. Liu, M.Y. Lou, Q. Ji, Sensing characteristics of femtosecond laser-induced long period gratings by filling cladding holes in photonic crystal fiber, J. Lightwave Technol 32 (12) (2014) 2287–2292.
[3] B. Wang, W.G. Zhang, Z.Y. Bai, L. Wang, L.Y. Zhang, Q. Zhou, L. Chen, T.Y. Yan, CO2-laser-induced long period fiber gratings in few mode fibers, IEEE Photonics Technol. Lett. 27 (2) (2015) 145–148.
[4] C. Li, C.R. Liao, J. Wang, Z.Y. Li, Y. Wang, J. He, Z.Y. Bai, Y.P. Wang, Femtosecond laser microprinting of a polymer fiber Bragg grating for high-sensitivity temperature measurements, Opt. Lett. 43 (14) (2018) 3409–3412.
[5] J. Deng, D.N. Wang, Construction of cascaded Fabry-Perot interferometers by four in-fiber mirrors for high-temperature sensing, Opt. Lett. 44 (5) (2019) 1289–1292.
[6] Q.H. Wang, H. Zhang, D.N. Wang, Cascaded multiple Fabry-Perot interferometers fabricated in no-core fiber with a waveguide for high-temperature sensing, Opt. Lett. 44 (21) (2019) 5145–5148.
[7] H.L. Lu, Y.L. Yue, J. Du, L.P. Shao, T.Y. Wu, J. Pan, J.H. Hu, Temperature and liquid refractive index sensor using P-D fiber structure-based Sagnac loop, Opt. Express 26 (15) (2018) 18920–18927.
[8] E. Reyes-Vera, C.M.B. Cordeiro, P. Torres, Highly sensitive temperature sensor using a Sagnac loop interferometer based on a side-hole photonic crystal fiber filled with metal, Appl. Opt. 56 (2) (2017) 156–162.
[9] M. Sun, B. Xu, X.Y. Dong, Y. Li, Optical fiber strain and temperature sensor based on an in-line Mach-Zehnder interferometer using thin-core fiber, Opt. Commun. 285 (18) (2012) 3721–3725.
[10] J.E. Antonio-Lopez, Z.S. Eznaveh, P. Likamwa, A. Schulzgen, R. Amezcua-Correa, Multicore fiber sensor for high-temperature applications up to 1000 ℃, Opt. Lett 39 (15) (2014) 4309–4312.
[11] W.W. Li, D.N. Wang, Femtosecond laser inscribed straight waveguide in no-core fiber for in-line Mach-Zehnder interferometer construction, Opt. Lett. 43 (14) (2018) 3405–3408.
[12] Z.D. Zhu, L. Liu, Z.H. Liu, Y. Zhang, Y.X. Zhang, Surface-plasmon-resonance-based optical-fiber temperature sensor with high sensitivity and high figure of merit, Opt. Lett. 42 (15) (2017) 2948–2951.
[13] Y. Wang, Q. Huang, W. Zhu, M. Yang, E. Lewis, Novel optical fiber SPR temperature sensor based on MMF-PCF-MMF structure and gold-PDMS film, Opt. Express 26 (2) (2018) 1910–1917.
[14] X. Zhan, Y.P. Liu, M. Tang, L. Ma, R.X. Wang, L. Duan, L. Gan, C. Yang, W.J. Tong, S.N. Fu, D.M. Liu, Z.Y. He, Few-mode multicore fiber enabled integrated Mach-Zehnder interferometers for temperature and strain discrimination, Opt. Express 26 (12) (2018) 15332–15342.
[15] K.M. Yang, J. He, Y. Wang, S. Liu, C.R. Liao, Z.Y. Li, G.L. Yin, B. Sun, Y.P. Wang, Ultrasensitive temperature sensor based on a fiber Fabry-Perot interferometer created in a mercury-filled silica tube, IEEE Photonics J. 7 (6) (2015).
[16] Y. Wang, M.W. Yang, D.N. Wang, C.R. Liao, Selectively infiltrated Photonic Crystal Fiber with ultrahigh temperature sensitivity, IEEE Photonics Technol. Lett. 23 (20) (2011) 1520–1522.
[17] R. Yang, Y.S. Yu, Y. Xue, C. Chen, C. Wang, F. Zhu, B.L. Zhang, Q.D. Chen, H. B. Sun, A highly sensitive temperature sensor based on a liquid-sealed S-tapered fiber, IEEE Photonics Technol. Lett. 25 (9) (2013) 829–832.
[18] Y. Xue, Y.S. Yu, R. Yang, C. Wang, C. Chen, J.C. Guo, X.Y. Zhang, C.C. Zhu, H. B. Sun, Ultrasensitive temperature sensor based on an isopropanol-sealed optical microfiber taper, Opt. Lett. 38 (8) (2013) 1209–1211.
[19] Y. Jiang, Z. Fang, Y. Du, E. Lewis, G. Farrell, P. Wang, Highly sensitive temperature sensor using packaged optical microfiber coupler filled with liquids, Opt. Express 26 (1) (2018) 356–366.
[20] P. Pilla, P. Foglia Manzillo, M. Giordano, M.L. Korwin-Pawlowski, W.J. Bock, A. Cusano, Spectral behavior of thin film coated cascaded tapered long period gratings in multiple configurations, Opt. Express 16 (13) (2008) 9765–9780.
[21] Y.H.T. Charles, N.P. David, G.W. Alec, Modal characteristics of three-layered optical fiber waveguides: a modified approach, J. Opt. Soc. Am. A 6 (4) (1989) 555–563.
[22] Y.X. Zhang, A. Zhou, B.Y. Qin, H.C. Deng, Z.H. Liu, J. Yang, L.B. Yuan, Refractive index sensing characteristics of single-mode fiber-based modal interferometers, J. Lightwave Technol 32 (9) (2014) 1734–1740.
[23] Y. Chen, F. Xu, Y.Q. Lu, Teflon-coated microfiber resonator with weak temperature dependence, Opt. Express 19 (23) (2011) 22923–22928.
[24] S.J. Qiu, Y. Chen, F. Xu, Y.Q. Lu, Temperature sensor based on an isopropanol-sealed photonic crystal fiber in-line interferometer with enhanced refractive index sensitivity, Opt. Lett. 37 (5) (2012) 863–865.
[25] M. Deng, L.G. Liu, Y. Zhao, G.L. Yin, T. Zhu, Highly sensitive temperature sensor based on an ultra-compact Mach-Zehnder interferometer with side-opened channels, Opt. Lett. 42 (18) (2017) 3549–3552.
[26] X.W. Guan, X.Y. Wang, L.H. Frandsen, Optical temperature sensor with enhanced sensitivity by employing hybrid waveguides in a silicon Mach-Zehnder interferometer, Opt. Express 24 (15) (2016) 16349–16356.
[27] S.H. Liu, H.L. Zhang, L.T. Li, L.M. Xiong, P.P. Shum, Liquid core fiber interferometer for simultaneous measurement of refractive index and temperature, IEEE Photonics Technol. Lett. 31 (2) (2019) 189–192.
[28] C.Y. He, J.B. Fang, Y.N. Zhang, Y. Yang, J.H. Yu, J. Zhang, H.Y. Guan, W.T. Qiu, P. J. Wu, J.L. Dong, H.H. Liu, J.Y. Tang, W.G. Zhu, N. Arsad, Y. Xiao, Z. Chen, High performance all-fiber temperature sensor based on coreless side-polished fiber wrapped with polydimethylsiloxane, Opt. Express 26 (8) (2018) 9686–9699.
[29] K. Mullaney, R. Correia, S.E. Staines, S.W. James, R.P. Tatam, Monitoring techniques for the manufacture of tapered optical fibres, Appl. Opt. 54 (28) (2015) 8531–8536.